START

000020

WATER RESOURCES RESEARCH, VOL. 20, NO. 8, PAGES 1099–1115, AUGUST 1984

NOTICE: This material may be protected by copyright law (Title 17 U.S. Code)

Techniques for Making Finite Elements Competitve in Modeling Flow in Variably Saturated Porous Media

P. S. HUYAKORN, AND S. D. THOMAS

GeoTrans, Inc., Reston, Virgina

B. M. THOMPSON

Intera, Houston, Texas

A Galerkin finite element formulation is developed for the numerical simulation of water flow in variably saturated soil systems. Included in this formulation is a solution strategy based on Picard and Newton-Raphson algorithms. Both algorithms are designed especially to cope with severely nonlinear field problems. The two algorithms are formulated for both rectangular and triangular elements. The element matrices are evaluated in a simple and efficient manner using a technique referred to as the "influence coefficient" technique. This technique avoids numerical integration and leads to a substantial saving of computational cost. Four examples are presented to demonstrate the effectiveness of the present finite element approach. These examples show that the nonlinear solution schemes are capable of accomodating cases involving large variations in the saturated hydraulic conductivity, as well as highly nonlinear soil moisture characteristics. A comparative study of the Picard and the Newton-Raphson algorithms is also provided. The study indicates that despite the higher cost per iteration of the Newton-Raphson scheme, it usually requires a substantially smaller number of iterations than the Picard scheme. In some instances where convergence difficulties are experienced with the latter scheme, it is desirable to use the Newton-Raphson scheme in order to obtain a cost-effective solution to the problem.

6 9 8 9 1 7 1 2 4 1 2

INTRODUCTION

In recent years, problems involving water flow and solute transport in variably saturated porous media have received increasing attention. One primary reason for this is the need to evaluate the suitability of a site for near surface disposal of toxic wastes. Another reason is the need to evaluate the impact of an existing waste disposal site on the groundwater system and its environment. Both types of evaluation require a thorough understanding of water flow and contaminant migration in soil materials. An effective way to develop such an understanding is by means of computer simulation using numerical models.

This paper is the first in a series of three papers that deal with the development and application of two- and three-dimensional finite element models. These models have been designed to provide cost-effective solutions to variably saturated flow and solute transport problems. Our prime motivation in presenting this work is to provide innovative techniques for enhancing the efficiency of the Galerkin finite element approach, thus making it more attractive to use in solving complex field problems. To achieve the main goal, it is essential to address four fundamental issues pertaining to two- and three-dimensional finite element computations. These issues concern the following: (1) the evaluation of element matrices, (2) the formulation of nonlinear solution algorithms capable of treating field problems with severely nonlinear flow conditions, (3) the formulation of a matrix assembly and solution scheme that permits large three-dimensional problems, containing probably several thousand unknowns, to be solved efficiently, and (4) the formulation of a reliable and efficient mass balance computational scheme.

The first issue is important because the number of repetitions of element matrix computation is usually very large in a long-term transient simulation, particularly when nonlinearities are involved. Thus there is a need to develop an efficient technique for element matrix generation. To be effective, such a technique should avoid costly numerical integration.

The second issue merits serious consideration because most of the earlier nonlinear schemes have difficulties coping with certain practical cases involving severely nonlinear soil moisture characteristics and large variations of hydraulic properties.

The third issue is critical when one attempts to apply the Galerkin method to complex three-dimensional field problems. The conventional procedure for element matrix formulation and assembly leads to a system of algebraic equations with a very large matrix bandwidth. Such a system is extremely costly to solve. Consequently, there is a need for a better matrix solution approach.

The fourth issue is also important, although not critical. Our literature survey indicates that in most of the previous work, mass balance computation is not provided as part of the finite element formulation of flow and transport problems. Only two recent papers [*Yeh*, 1981; *Yeh and Ward*, 1981] attempt to address the mass computational problem. However, the mass balance algorithms provided in these papers require excessive computational effort.

PURPOSE AND SCOPE

The present paper deals with two-dimensional variably saturated flow problems and focuses on the first two issues stated earlier. The second and third papers will deal with two-dimensional transport and three-dimensional flow and transport problems in their respective order. These forthcoming papers will also focus on the third and fourth issues.

Several researchers have applied finite element techniques to two-dimensional saturated-unsaturated flow problems. Among these are *Neuman* [1973], *Neuman et al.* [1974],

Copyright 1984 by the American Geophysical Union.

Paper number 4W0647.
0043-1397/84/004W-0647$05.00

Reeves and Duguid [1976], *Bruch* [1977], *Frind et al.* [1977], *Yeh and Ward* [1980], and *Cooley* [1983]. In most of these previous studies (with the exception of *Cooley* [1983]), nonlinearities were treated using standard Picard solution algorithms. Although such algorithms are simple to derive, difficulties usually arise when one attempts to apply them to certain field problems such as those considered in the present study.

In order to deal with a wider range of field conditions, an improved Picard algorithm and a Newton-Raphson algorithm are provided in this paper. (The Newton-Raphson algorithm is included because it proves to be a good alternative method to use in certain instances where convergence difficulties are encountered with the Picard method.) The two algorithms have been designed to accommodate a wide range of nonlinear soil moisture characteristic curves. In contrast to most of the previous studies [e.g., *Neuman*, 1973; *Reeves and Duguid*, 1976], which used either triangular elements or quadrilateral elements, we use both rectangular and triangular elements in this paper. A simple technique called "the influence coefficient matrix technique" is presented for evaluating element matrices resulting from the Picard and the Newton-Raphson algorithms. This technique avoids numerical integration and thus enables element matrices to be computed in a simple and cost-effective manner. Furthermore, the use of the chord slope approximation of the moisture-capacity term leads to improved convergence of the nonlinear iterations.

GOVERNING EQUATIONS

Consider a situation involving two-dimensional isothermal flow of liquid water in a partially saturated porous medium. Assuming that the role of the air phase is insignificant, the water flow problem can be described by the modified form of Richards' equation [see *Richards*, 1931; *Cooley*, 1971; *Braester et al.*, 1971]:

$$\frac{\partial}{\partial x_i}\left[K_{ij}k_{rw}\left(\frac{\partial\psi}{\partial x_j}+e_j\right)\right]=\left(S_wS_s+\phi\frac{dS_w}{d\psi}\right)\frac{\partial\psi}{\partial t}-q \qquad (1)$$

where ψ is the pressure head, K_{ij} is the saturated hydraulic conductivity tensor, k_{rw} is the relative permeability with respect to the liquid water phase, $x_i (i = 1, 2)$ are spatial coordinates, t is elapsed time, e_j is the unit vector in the direction of the x_2 coordinate (assumed to be vertically upward), S_w is water saturation, S_s is the specific storage, ϕ is porosity, and q is the volumetric flow rate via sources (or sinks) per unit volume of the medium.

It is apparent from (1) that we have posed the problem using pressure head and water saturation as dependent variables. These two variables are related by a nonlinear constitutive relationship which depends on the type of soil. The relative permeability k_{rw} is also a nonlinear function which can be expressed in terms of either water saturation or pressure head. In this work it is assumed that k_{rw} is written in terms of water saturation. It should also be noted that q, which represents the source or sink term of (1), may also be nonlinear (e.g., in a case involving evapotranspiration or water uptake by plants).

For the sake of convenience, (1) is rewritten in the form

$$\frac{\partial}{\partial x_i}\left[K_{ij}k_{rw}\left(\frac{\partial\psi}{\partial x_j}+e_j\right)\right]=\eta\frac{\partial\psi}{\partial t}-q \qquad (2)$$

where η is an overall storage coefficient, defined as

$$\eta=S_wS_s+\phi\frac{dS_w}{d\psi} \qquad (3)$$

The initial and boundary conditions associated with (2) can be expressed as

$$\psi(x_i, 0)=\psi_0(x_i) \qquad (4)$$

$$\psi(x_i, t)=\bar{\psi} \qquad \text{on } B_1 \qquad (5)$$

and

$$V_in_i=-V_n \qquad \text{on } B_2 \qquad (6)$$

where ψ_0 is the initial head value, B_1 is the portion of the flow boundary where ψ is prescribed as $\bar{\psi}$, B_2 is the portion of the flow boundary where the outward fluid flux is prescribed as $-V_n$, and n_i is the outward unit vector normal to the boundary B_2.

In this work the solution of (2) subject to (4)–(6) is formulated using the Galerkin finite element method. When the distributions of ψ and S_w have been determined, Darcy velocity components are computed using the following equation

$$V_i=-K_{ij}k_{rw}\left(\frac{\partial\psi}{\partial x_j}+e_j\right) \qquad (7)$$

GALERKIN APPROXIMATION

To approximate the flow equation by the Galerkin finite element method, let the pressure head function ψ be approximated by a trial function of the form

$$\hat{\psi}(x_i, t)=N_J(x_i)\psi_J(t) \qquad J=1, 2, \cdots, n \qquad (8)$$

where $N_J(x_i)$ and $\psi_J(t)$ are basis functions and nodal values of ψ at time t, respectively, n is the number of nodes in the finite element network, and repeated indices imply nodal summation. By applying the Galerkin finite element procedure to (2) and transforming the second order derivative term (for details, see *Huyakorn and Pinder* [1983]), one obtains

$$\int_R K_{ij}k_{rw}\frac{\partial N_I}{\partial x_i}\frac{\partial N_J}{\partial x_j}\psi_J\,dR+\int_R K_{ij}k_{rw}\frac{\partial N_I}{\partial x_i}e_j\,dR+\int_R \eta N_IN_J\frac{d\psi_J}{dt}\,dR-\int_B K_{ij}k_{rw}\left(\frac{\partial\psi}{\partial x_j}+e_j\right)n_i\,dB-\int_R N_Iq\,dR=0 \qquad I=1, 2, \cdots, n \qquad (9)$$

where R is the solution domain with boundary B.

Recognizing that the basis functions are piecewise continuous over each element, (9) is now written as

$$A_{IJ}\psi_J+B_{IJ}\frac{d\psi_J}{dt}-F_I=0 \qquad I=1, 2, \cdots, n \qquad (10)$$

with the matrix coefficients defined as

$$A_{IJ}=\sum_e A_{IJ}^e=\sum_e\int_{R^e}K_{ij}k_{rw}\frac{\partial N_I}{\partial x_i}\frac{\partial N_J}{\partial x_j}\,dR \qquad (11)$$

$$B_{IJ}=\sum_e B_{IJ}^e=\sum_e\int_{R^e}\eta N_IN_J\,dR \qquad (12)$$

$$F_I=\sum_e F_I^e=\sum_e\left(\int_{R^e}-K_{ij}k_{rw}\frac{\partial N_I}{\partial x_i}e_j\,dR\right)+\int_R N_Iq\,dR+\sum_e\left(\int_{B^e}V_nN_I\,dB\right) \qquad (13)$$

where R^e is the element subdomain with boundary B^e, V_n denotes the normal Darcy flux intensity at the boundary, and the summation is performed over the total number of ele-

ments. The sign convention for V_n is chosen to be the same as q. That is, V_n is positive for inward flow and negative for outward flow.

SOLUTION STRATEGY

Equation (10) is a system of time-independent integrodifferential equations that are nonlinear because the matrix elements, A_{IJ} and B_{IJ}, are functions of the nodal unknowns, ψ_J. To obtain a cost-effective solution of such a nonlinear system, the following solution strategy is adopted:

1. Treat the nonlinearities using an implicit Picard iterative scheme or a more strongly convergent Newton-Raphson iterative scheme designed especially to avoid convergence difficulties usually encountered when certain nodes are being desaturated. Neither of these iterative schemes requires artificial lumping of the mass matrix defined in (12).
2. Use simple rectangular and triangular elements and avoid costly numerical intergration in computing element matrices and the right-hand-side vector. The numerical integration can be avoided by computing the element matrices using an influence coefficient technique described in a subsequent section.
3. Perform time marching using an automatic scheme that permits the time step value to be increased logarithmically and permits the time step to be cut back and the solution continued when the maximum number of iterations allowed is exceeded.
4. After convergence of the numerical solution, compute element velocities using simple formulas that require minimal computational effort.

Picard Scheme

In the Picard iterative scheme, time integration of (10) is performed in a standard manner using a finite difference approximation of the time derivative. After rearrangement of the terms, the following system of algebraic equations is obtained:

$$\left(\omega A_{IJ}^{k+\omega} + \frac{B_{IJ}^{k+\omega}}{\Delta t_k}\right)\psi_J^{k+1} = F_I^{k+\omega} + (\omega - 1)A_{IJ}^{k+\omega}\psi_J^k + \frac{B_{IJ}^{k+\omega}}{\Delta t_k}\psi_J^k \qquad (14)$$

where ω is a time weighting factor, superscrips k and $k+1$ denote the previous and current time levels respectively, and Δt_k is the kth time increment, $\Delta t_k = t_{k+1} - t_k$.

In this work, either the time-centered Crank-Nicolson scheme or the fully implicit backward difference time stepping scheme is adopted, and the value of ω is set to either 0.5 or 1. Within each time step, iterations are performed to achieve a stable numerical solution. For each iteration the most recent nodal values, $\psi_J^{k+\omega} = (1-\omega)\psi_J^k + \omega\psi_J^{k+1}$, are used to compute coefficient matrices and right-hand-side vector. Experience indicates that to obtain good convergence, caution must be exercised in the computation of the moisture capacity term, $\phi dS_w/d\psi$, of (3). Rather than using the tangent slope of the water saturation versus pressure head curve, the term $dS_w/d\psi$ is computed using the following chord slope formula:

$$\frac{dS_w}{d\psi} = \frac{S_w^{r+1} - S_w^r}{\psi^{r+1} - \psi^r} \qquad (15)$$

where $r+1$ and r denote current and previous iteration levels, and the absolute head difference $|\psi^{r+1} - \psi^r|$ is determined

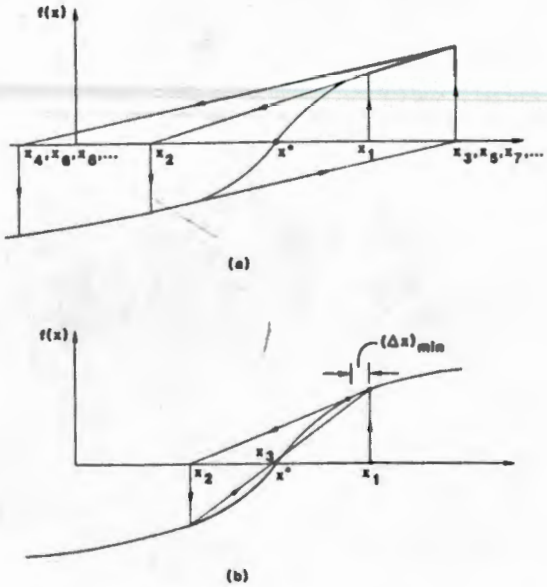

Fig. 1. Iterative solution of nonlinear equation $f(x) = 0$. (*a*) Newton-Raphson scheme. (*b*) Chord slope scheme.

such that it is no less than a certain small tolerance $(\Delta\psi)_{min}$ that may be chosen arbitrarily.

To illustrate how the use of chord slope projection can drastically improve convergence of the nonlinear iterations, consider a simple case illustrated in Figure 1. Despite the fact that this case involves the Newton-Raphson type solution of a one-variable problem, $f(x) = 0$, it provides a good demonstrative example. In Figure 1*a* it is seen that the tangent slope iterative procedure, which starts with an initial guess x_1, fails to converge when $f(x)$ takes an S shape and the correct solution x^* is at the inflection point of the curve. To overcome the convergence difficulty, the chord slope projection is applied, as shown in Figure 1*b*. It can be seen that by starting with the same initial value, x_1, convergence to the correct solution is achieved after three iterations.

The above discussion can be extended to the variably saturated flow problem because this problem is an iterative solution of (14) which can be expressed in the form

$$f_I(x_1, x_2, \cdots, x_n) = 0 \qquad I = 1, 2, \cdots, n \qquad (16)$$

where $x_I \equiv \psi_I^{k+1}$.

The function f_I usually exhibits inflection due to the fact that the relationship of S_w versus ψ is usually an S shape curve. Thus it is not surprising to encounter convergence difficulties if the tangent slope evaluation of $dS_w/d\psi$ is used in conjunction with the Picard or the Newton-Raphson solution of (14). In a manner similar to that shown in Figure 1, the convergence failure is manifested as oscillations about the true solution. To circumvent such difficulties, we decided to adopt the chord slope based iterative scheme. For the Picard scheme, the chord slope evaluation is performed for $dS_w/d\psi$. For the Newton-Raphson, which is elaborated in the next section, the chord-slope evaluation is performed for both $dS_w/d\psi$ and dk_{rw}/dS_w.

Another significant feature of the present nonlinear formulation is the use of extrapolation formulas for estimating nodal values, ψ^{k+1}, thereby further enhancing convergence of the iterative process. At the start of a new time level, an initial

estimate of ψ^{k+1} is obtained from

$$\psi_j^{k+1} = \psi_j^k \qquad k = 1 \tag{17a}$$

$$\psi_j^{k+1} = \psi_j^k + (\psi_j^k - \psi_j^{k-1})\Delta t_k / 2\Delta t_{k-1} \qquad k = 2 \tag{17b}$$

$$\psi_j^{k+1} = \psi_j^k + (\psi_j^k - \psi_j^{k-1}) \frac{\log (t_{k+1}/t_k)}{\log (t_k/t_{k-1})} \qquad k > 2 \tag{17c}$$

Equations (17*b*) and (17*c*) were used by *Cooley* [1971]. One other feature of our proposed Picard solution algorithm is a provision for combining central and backward difference temporal approximations. The combination is made in the following manner. For those finite elements that are in the unsaturated zone, the time weighting coefficient ω is set equal to 0.5, thus resulting in the use of central difference approximation in time. For the remaining elements that are in the saturated zone, ω is set equal to 0.5 or 1, depending on whether compressibility of the porous medium, the S_s term of (3), is taken into account. The use of backward difference ($\omega = 1$) is desirable when the storage term is zero and the governing equation (2) becomes an elliptic equation [*Neuman et al.*, 1974].

For each iteration a system of linearized algebraic equations is derived. After proper incorporation of boundary conditions the linear system can be solved using a direct equation solver that takes into account the symmetric and banded feature of the global coefficient matrix. Updating of matrix elements is performed by recomputing values of relative permeability and overall storage coefficient of the mass accumulation terms. Iterations are performed until the successive change of pressure head values is within a prescribed head tolerance.

Matrix Computation for Rectangular Elements

It is apparent that the Picard algorithm presented above requires computation of coefficient matrices $[A]$ and $[B]$ and the right-hand-side vector $\{F\}$ of (14) for each iterative solution performed within each time step. Because the total number of repetitions of such computation can be up to several hundred or even a few thousand in a long-term simulation of a field problem, it is desirable to minimize the computational effort required to obtain element matrices, $[A]^e$ and $[B]^e$, and the element right-hand-side vector $\{F\}^e$. This is accomplished by using an influence coefficient technique described below.

Consider the rectangular element with the local node numbering shown in Figure 2*a*. Let us assume that x and y correspond to x_1 and x_2 coordinates and that the coordinate axes are parallel to the directions of the principal components of the hydraulic conductivity tensor. Using these assumptions and (11), one obtains

$$A_{IJ}^e = \int_{R^e} \left(K_{xx}k_{rw} \frac{\partial N_I}{\partial x}\frac{\partial N_J}{\partial x} + K_{yy}k_{rw} \frac{\partial N_I}{\partial y}\frac{\partial N_J}{\partial y} \right) dR$$
$$\simeq \langle K_{xx}k_{rw}\rangle \int_{R^e} \frac{\partial N_I}{\partial x}\frac{\partial N_J}{\partial x}\, dR + \langle K_{yy}k_{rw}\rangle \int_{R^e} \frac{\partial N_I}{\partial y}\frac{\partial N_J}{\partial y}\, dR \tag{18a}$$

where $\langle K_{xx}k_{rw}\rangle$ and $\langle K_{yy}k_{rw}\rangle$ are values of $K_{xx}k_{rw}$ and $K_{yy}k_{rw}$ at the element centroid. Note that the centroidal value approximations of $K_{xx}K_{rw}$ and $K_{yy}K_{rw}$ are used in preference to functional representations in order to simplify the integration and obtain a simple expression for element matrix $[A]^e$. Such approximations are usually adequate when used in conjunction with a sufficiently refined finite element mesh.

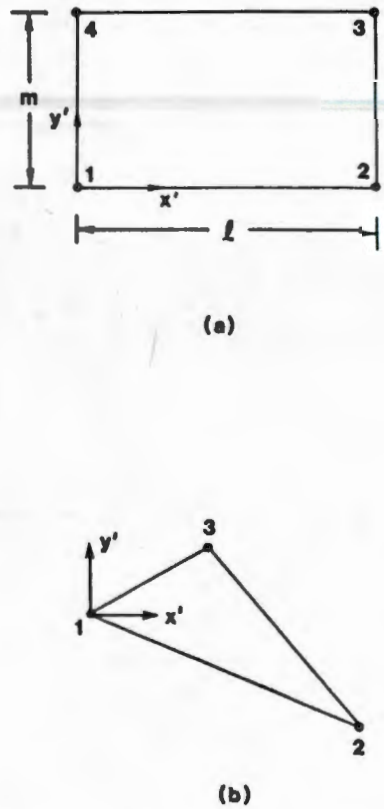

Fig. 2. Local node numbering and coordinate systems for (*a*) rectangular element and (*b*) triangular element.

In matrix form, (18*a*) can be written as

$$[A]^e = \langle K_{xx}k_{rw}\rangle \frac{m}{l}[A^{xx}]^e + \langle K_{yy}k_{rw}\rangle \frac{l}{m}[A^{yy}]^e \tag{18b}$$

where l and m are the dimensions of the rectangular element, and $[A^{xx}]^e$ and $[A^{yy}]^e$ are matrix coefficients that are independent of the dimensions of the rectangle.

Because $[A^{xx}]^e$ and $[A^{yy}]^e$ are independent of the element dimensions, they are referred to as "influence coefficient" matrices. The expressions of $[A^{xx}]^e$ and $[A^{yy}]^e$ are given in Appendix A. In a similar manner, it can be shown that the element matrix $[B]^e$ of (12) can be computed from

$$[B]^e = \frac{lm}{4}\langle \eta \rangle [M]^e \tag{19}$$

where $\langle \eta \rangle$ is the value of η at the element centroid and $[M]^e$ is another influence coefficient matrix, given in Appendix A.

As can be seen from the appendix, the three influence coefficient matrices are extremely simple and require virtually no computational effort to evaluate. Furthermore, each of these matrices has an interesting property: the sum across any row or column is equal to a constant, zero for $[A^{xx}]^e$ and $[A^{yy}]^e$ and unity for $[M]^e$. This property can be used as a quick means for checking the result of element matrix computation.

Assuming, for the time being, that the sink (or source) and boundary flux terms are zero and that the y coordinate axis points vertically upward, the right-hand-side vector $\{F\}^e$ can

also be easily computed from

$$\{F\}^e = -\frac{l}{2}\langle K_{yy}k_{rw}\rangle\{F_y\}^e \tag{20}$$

where $\{F_y\}^e$ is an influence vector given in Appendix A.

In the case where a boundary segment (say, segment 1–2 in Figure 2*a*) corresponds to the flux boundary, the boundary flux term exists and the last term in (13) can be written in matrix notation as

$$\int_{B^e} V_n\{N\}^e\, dB = \frac{l}{2}\begin{Bmatrix}(2V_{n1} + V_{n2})/3\\(V_{n1} + 2V_{n2})/3\\0\\0\end{Bmatrix} \tag{21}$$

where V_{n1} and V_{n2} are normal flux values at node 1 and 2, respectively, and l is the length of the boundary segment.

Finally, if sinks or sources are present in the flow domain, the sink or source term in (13) depends on the type of sink or source function. For the case involving point sinks and sources, the general expression for q is

$$q = \sum_{l'=1}^{n_w} Q_{l'}\delta(x - x_{l'}, y - y_{l'}) \tag{22}$$

where n_w is the number of sinks and sources. When (22) is used, the sink (or source) term in (13) becomes

$$\sum_e \int_{R^e} N_l q\, dR = \sum_e Q_l^e = Q_l \tag{23}$$

For the case involving distributed sources, q can be represented using linear interpolation functions and the integral can also be evaluated in a simple manner.

Matrix Computation for Triangular Elements

To handle a flow region with complex geometry, it is desirable to use rectangular elements in combination with triangular elements, particularly in the zones where mesh expansion or contraction is required or where boundary geometry cannot be accurately represented by the use of rectangular elements alone. A typical example showing an effective utilization of combined rectangular and triangular elements is depicted in Figure 3. Coefficient matrices for triangular elements can also be constructed by using the influence coefficient technique described previously.

Consider the typical triangular element with the local node numbering shown in Figure 2*b*. The 3 × 3 element matrix $[A]^e$ resulting from the Galerkin approximation of the flow equation is obtainable from

$$[A]^e = \Delta(\langle k_{xx}k_{rw}\rangle[A^{xx}]^e + \langle K_{yy}k_{rw}\rangle[A^{yy}]^e) \tag{24a}$$

where $[A^{xx}]^e$ and $[A^{yy}]^e$ are influence coefficient matrices given in Appendix B, $\langle K_{xx}k_{rw}\rangle$ and $\langle K_{yy}k_{rw}\rangle$ are values of the components of the hydraulic conductivity tensor at the centroid of the triangle, and Δ is the triangle area. Note again that the sum across each row and each column of these matrices is equal to zero. In addition, considerably more computational effort is required to generate these 3 × 3 matrices for triangular elements as compared to the 4 × 4 influence coefficient matrices for rectangular elements.

Similarly, the mass matrix $[B]^e$ and the right-hand-side vector of the triangle can be generated from the formulas

$$[B]^e = \frac{\Delta}{3}\langle\eta\rangle\,[M]^e \tag{24b}$$

$$\{F\}^e = -\Delta(\langle K_{yy}k_{rw}\rangle\{F_y\}^e) \tag{24c}$$

where $[M]^e$ and $\{F_y\}^e$ are also given in Appendix B.

Newton-Raphson Scheme

In certain situations where the relative permeability and water saturation functions are very highly nonlinear, convergence difficulties may be encountered in solving the flow equation by using the Picard iterative method. To overcome this problem, the Newton-Raphson method should be considered. The Newton-Raphson procedure has been widely used in conjunction with finite difference techniques to solve variably-saturated flow problems. Examples of its application can be found in the work of *Brutsaert* [1971]. Unfortunately, for the nonlinear flow equation considered in the present investigation, most finite element solution schemes reported in the literature are based on Picard's iterations. In view of this, it is appropriate to provide herein a comprehensive derivation of the Newton-Raphson algorithm developed in the present investigation.

Let G_l denote the left-hand side of the system of ordinary differential equations (10) resulting from the Galerkin finite element approximation of the variably saturated flow equation. Thus G_l can be expressed as

$$G_l \equiv A_{lJ}\psi_J + B_{lJ}\frac{d\psi_J}{dt} - F_l = 0 \qquad l = 1, \cdots, n \tag{25}$$

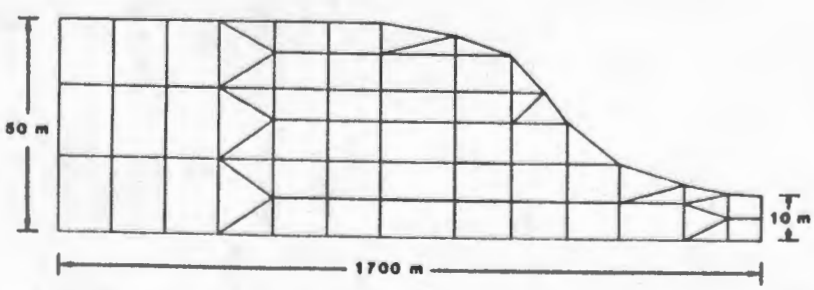

Fig. 3. Example illustrating how rectangular and triangular elements can be utilized effectively to represent a region with irregular geometry.

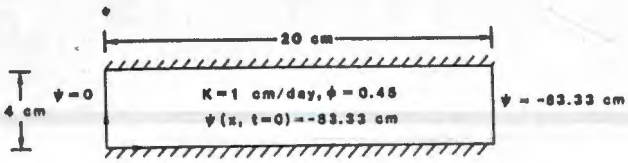

Fig. 4. Schematic description and data for the test problem in example 1.

For the typical rectangular element (Figure 2*a*) the expression for G_I^e can be written in the form

$$G_I^e = A_{IJ}^e\psi_J + \left(\frac{lm}{4}\right)S_s\bar{S}_w M_{IJ}^e \frac{d\psi_J}{dt} + \left(\frac{\phi lm}{4}\right)\left(\frac{d\bar{S}_w}{d\bar{\psi}}\frac{d\bar{\psi}}{dt}\right)u_I - F_I^e = 0 \qquad (26)$$

$$I = 1, 2, 3, 4$$

where A_{IJ}^e and M_{IJ}^e are elements of the element matrices $[A]^e$ and $[M]^e$, $\bar{S}_w$ and $\bar{\psi}$ are centroidal values of water saturation and pressure head functions, respectively, and $u_I = 1$ for $I = 1$ through 4. Note that $\bar{\psi} = \frac{1}{4}(\psi_1 + \psi_2 + \psi_3 + \psi_4)$, and use of the chain rule of differentiation $\partial\bar{S}_w/\partial t$ has been replaced by $(d\bar{S}_w/d\bar{\psi})(\partial\bar{\psi}/dt)$.

Application of the Newton-Raphson procedure to (25), written in its fully implicit finite difference form, yields [see *Huyakorn and Pinder*, 1983]

$$G_I^{r+1} = G_I^r + \left(\frac{\partial G_I}{\partial \psi_J}\right)^r \Delta\psi_J^{r+1} = 0 \qquad I = 1, 2, \cdots, n \qquad (27)$$

where r and $r + 1$ denote previous and present iteration levels at the current time value, $\Delta\psi_J^{r+1}$ is defined as

$$\Delta\psi_J^{r+1} = \psi_J^{r+1} - \psi_J^r \qquad (28)$$

and the Jacobian is given by

$$\frac{\partial G_I}{\partial \psi_J} = A_{IJ} + \psi_L \frac{\partial A_{IL}}{\partial \psi_J} + \frac{B_{IJ}}{\Delta t_k} - \frac{\partial F_I}{\partial \psi_J} \qquad (29)$$

in which L is a dummy nodal subscript and Δt_k is the time increment. Equation (27) can be written in the form

$$\sum_e \left\{(G_I^r) + \left(\frac{\partial G_I}{\partial \psi_J}\right)^r \Delta\psi_J^{r+1}\right\}^e = 0 \qquad I = 1, 2, \cdots, n \qquad (30)$$

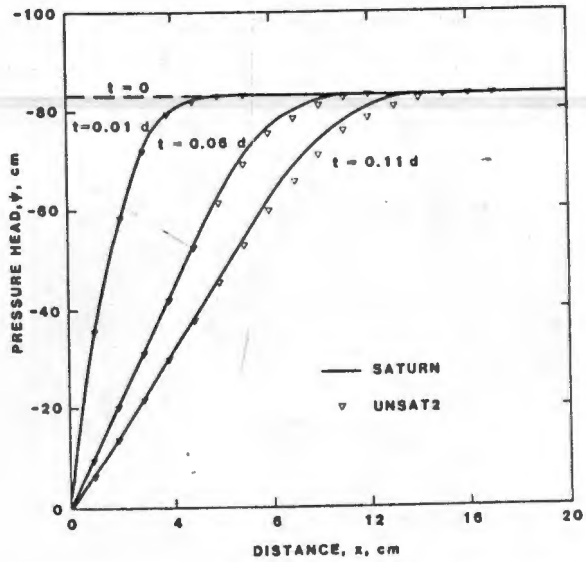

Fig. 6. Comparison of pressure head profiles computed by SATURN and UNSAT2.

For individual finite elements, the Jacobian can be expressed in the form

$$\left(\frac{\partial G_I}{\partial \psi_J}\right)^e = A_{IJ}^e + A_{IJ}^{*e} + B_{IJ}^{*e} + F_{IJ}^{*e} \qquad I, J = 1, 2, 3, 4 \qquad (31)$$

where A_{IJ}^e corresponds to the matrix elements of the Picard iterative method, and A_{IJ}^{*e}, B_{IJ}^{*e}, and F_{IJ}^{*e} are given by

$$A_{IJ}^{*e} \equiv \psi_L \frac{\partial A_{IL}^e}{\partial \psi_J} = \left(\frac{\partial k_{rw}}{\partial \psi_J}\right)\left[K_{xx}\frac{m}{l}(A_{IL}^{xx})^e + K_{yy}\frac{l}{m}(A_{IL}^{yy})^e\right]\psi_L \qquad (32a)$$

$$B_{IJ}^{*e} = \left(\frac{lm}{4}\right)\left(\frac{S_s\bar{S}_w}{\Delta t_k}\right)M_{IJ}^e + \frac{\phi lm}{4\Delta t}\left(\frac{d\bar{S}_w}{d\bar{\psi}}\right)u_I^e \frac{\partial\bar{\psi}}{\partial\psi_J} = \left(\frac{lm}{4}\right)\left(\frac{S_s\bar{S}_w}{\Delta t_k}\right)M_{IJ}^e + \frac{\phi lm}{16\Delta t_k}\left(\frac{d\bar{S}_w}{d\bar{\psi}}\right)U_{IJ}^e \qquad (32b)$$

$$F_{IJ}^{*e} = \left(\frac{\partial k_{rw}}{\partial \psi_J}\right)\left[\left(\frac{l}{2}\right)F_{yI}^e\right] \qquad (32c)$$

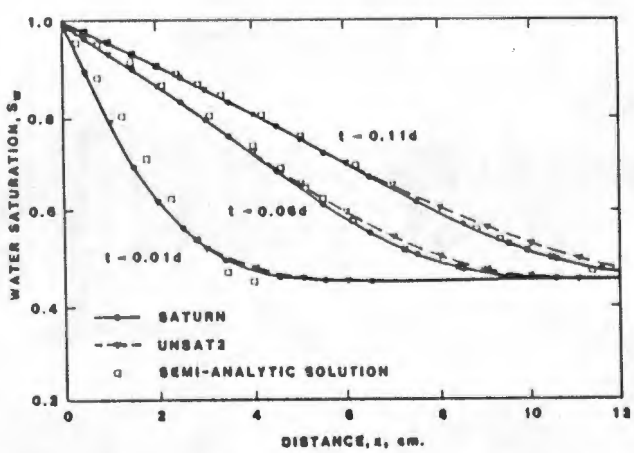

Fig. 5. Comparison of water saturation profiles obtained using SATURN, UNSAT2, and the semianalytical solution.

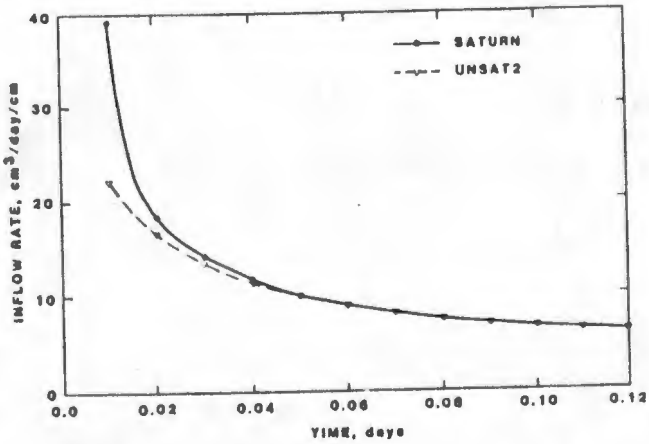

Fig. 7. Comparison of inflow rates computed by SATURN and UNSAT 2.

in which A_{IL}^{xx} and A_{IL}^{yy} are the components of the influence coefficient matrix in the x and y directions, respectively, and $U_{IJ} = 1$ for all I and J. Note that $\partial \bar{k}_{rw}/\partial \psi_J$ is evaluated using the chain rule as follows:

$$\frac{\partial \bar{k}_{rw}}{\partial \psi_J} = \left(\frac{d\bar{k}_{rw}}{d\bar{S}_w}\right)\left(\frac{d\bar{S}_w}{d\bar{\psi}}\right)\frac{\partial \bar{\psi}}{\partial \psi_J} = \frac{1}{4}\left(\frac{d\bar{k}_{rw}}{d\bar{S}_w}\right)\left(\frac{d\bar{S}_w}{d\bar{\psi}}\right) \tag{33}$$

By substituting for $(G_I^r)^e$, $(\partial G_I^r/\partial \psi_J)^e$ and $\Delta\psi_J^{r+1}$, (30) can be written at the element level as follows:

$$\begin{aligned}(A_{IJ}^e + A_{IJ}^{*e} + F_{IJ}^{*e} + B_{IJ}^{*e})\psi_J^{r+1} &= (A_{IJ}^{*e} + F_{IJ}^{*e} + B_{IJ}^{*e})\psi_J^r \\ &\quad - \left(\frac{lm}{4}\right)S_s\bar{S}_w\frac{M_{IJ}^e}{\Delta t_k}(\psi_J^r - \psi_J^k) \\ &\quad - \left(\frac{\phi lm}{4}\right)\left(\frac{\bar{s}_w u_I}{\Delta t_k}\right)(\bar{\psi}^r - \bar{\psi}^k) + (F_I^e)^r\end{aligned} \tag{34}$$

In matrix form, (34) becomes

$$\begin{aligned}([A]^e + [A']^e)\{\psi\}^{r+1} &= [A']^e\{\psi\}^r - \left(\frac{lm}{4}\right)\left(\frac{S_s\bar{S}_w}{\Delta t_k}\right) \\ &\quad \cdot [M]^e(\{\psi\}^r - \{\psi\}^k) \\ &\quad - \left(\frac{\phi lm}{4}\right)\cdot\frac{\bar{S}_w(\bar{\psi}^r - \bar{\psi}^k)}{\Delta t_k}\{u\} + (\{F\}^e)^r\end{aligned} \tag{35}$$

where $[A]^e$ is identical to the element matrix $[A]^e$ of the Picard scheme, and $[A']^e$ is defined as

$$[A']^e = [A^*]^e + [F^*]^e + [B^*]^e \tag{36}$$

The remaining coefficient matrices $[A^*]^e$, $[B^*]^e$, and $[F^*]^e$ are given in Appendix C, which provides a quick means for element matrix computation particularly if we note that the columns of $[A^*]^e$ are identical to one another.

For a typical triangular element (Figure 2*b*), one can also apply the above Newton-Raphson procedure and obtain an element matrix that takes the same form as (35) with the exception that the leading term $(lm/4)$ now becomes $(\Delta/3)$, and $[A^*]^e$, $[B^*]^e$, and $[F^*]^e$ are given in Appendix D.

It is apparent from Tables 3 and 4 that the element matrix $[A^*]^e$ is asymmetric, thus causing the global coefficient matrix of the Newton-Raphson scheme to be asymmetric. Indeed, this is the main drawback of the Newton-Raphson scheme as compared to the Picard scheme, which produces a symmetric global coefficient matrix.

Velocity and Nodal Flux Computation

After satisfactory convergence of the iterative solution has been achieved, it is necessary to compute Darcy velocity components if a subsequent analysis of the related solute transport problem is required. If the flow problem is time dependent, the velocity computation may have to be performed for many time steps. Thus it is desirable to use a simple algorithm that permits the velocity computation to be achieved in a cost-effective manner. For this reason we have developed simple formulas that enable values of Darcy velocity components at the centroid of a rectangular or a triangular element to be determined using minimal computational effort. For the typical rectangular element (Figure 2*a*) the centroidal values of x and y components of the Darcy velocity are given by

$$\langle V_x\rangle = \frac{\langle K_{xx}k_{rw}\rangle}{2l}(h_1 + h_4 - h_2 - h_3) \tag{37a}$$

$$\langle V_y\rangle = \frac{\langle K_{yy}k_{rw}\rangle}{2m}(h_1 + h_2 - h_3 - h_4) \tag{37b}$$

where h_I is the hydraulic head at node I. The value of h_I is simply the sum of ψ_I and the elevation of node I with respect to a given datum. For the triangular element shown in Figure 2*b*, $\langle V_x\rangle$ and $\langle V_y\rangle$ are given by

$$\langle V_x\rangle = \langle K_{xx}k_{rw}\rangle(\beta_1 h_1 + \beta_2 h_2 + \beta_3 h_3) \tag{38a}$$

$$\langle V_y\rangle = \langle K_{yy}k_{rw}\rangle(\gamma_1 h_1 + \gamma_2 h_2 + \gamma_3 h_3) \tag{38b}$$

where β and γ are geometric coefficients of the triangular element and are defined in Appendix B. In addition to Darcy velocity computation, computation of nodal flux values for the boundary or interior nodes at which the fluid flux is nonzero may also be required. Although there are several schemes for determining the nodal flux values, the scheme recommended is the procedure in which back-substitution into the global matrix equation is performed for certain rows that correspond to the specified nodes. For a more detailed discussion of this procedure, the reader is referred to *Huyakorn and Pinder* [1983].

ILLUSTRATIVE EXAMPLES

A computer code called SATURN has been developed to simulate two-dimensional flow and transport in variably saturated porous media. The flow module of this code is based on the Galerkin finite element technique and the nonlinear solution techniques described in the foregoing sections. To verify these techniques and demonstrate their capability to handle very highly nonlinear problems, we elect to use four examples and present them in this section. In the first example, the SATURN code was used to solve a simple hypothetical one-dimensional problem. The numerical result obtained was compared with the semianalytical solution of *Philip* [1955, 1969], as well as the finite element solution obtained using the UNSAT2 flow code documented in the previous work by *Neuman et al.* [1974]. In the remaining examples the SATURN code was used to analyze three realistic one- and two-dimensional flow problems involving inhomogeneous soil materials and very highly nonlinear constitutive relations.

Example 1: One-Dimensional Horizontal Flow in a Uniform Soil Slab

This problem concerns one-dimensional adsorption into a soil column with the two ends subject to constant heads (Figure 4). The main purpose is to check both the Picard and the Newton-Raphson iterative schemes. This was achieved by comparing our numerical solution with the semianalytical solution of *Philip* [1955, 1969] and the corresponding finite element solution obtained by running the UNSAT2 code. For the sake of convenience, linear constitutive relations of k_{rw} versus S_w and S_w versus ψ were used. These relations and values of their parameters are presented in Appendix E.

To obtain the numerical solutions, the flow region was discretized using a uniform grid consisting of 20 rectangular elements, each having Δx of 1 cm and Δy of 4 cm, where Δx and Δy are the nodal spacings in the x and y directions, respectively. The time discretization was performed also in a simple manner using a constant value of $\Delta t = 0.01$ days. Computed values of water saturation are presented in Figure 5 for three typical time values. Note that the result from the SATURN code was obtained using the Picard algorithm, and the water saturation values depicted correspond to the values at the element centroids, whereas the water saturation values given

TABLE 1. Net Inflow Rate and Cumulative Fluid Storage Computed by SATURN and UNSAT2 for the Test Problem in Example 1

Time, days	Inflow Rate per Unit Width, $cm^3/d/cm$		
	SATURN (Picard)	SATURN (Newton-Raphson)	UNSAT2 (Picard)
0.01	39.09	38.41	21.79
0.02	18.63	18.93	16.65
0.03	14.06	14.14	13.39
0.04	11.74	11.78	11.44
0.05	10.28	10.31	10.13
0.06	9.262	9.282	9.177
0.07	8.495	8.511	8.446
0.08	7.892	7.905	7.864
0.09	7.402	7.412	7.386
0.10	6.993	7.002	6.983
0.11	6.645	6.652	6.637
0.12	6.344	6.351	6.335
0.13	6.080	6.086	6.068
0.14	5.846	5.852	5.827
0.15	5.636	5.642	5.610

by the UNSAT2 code correspond to the values at the nodes. As can be seen at time values of 0.06 and 0.11 days, both finite element solutions agree quite well with the semianalytical solution. (The agreement between the finite element results and the semianalytical solution is not so good at the early time value, $t = 0.01$ d. This is to be expected because the selected time step value, $\Delta t = 0.01$, is too large to provide accurate approximation of such an early moisture distribution.) It is also evident that at later times the saturation profiles obtained from the SATURN code are slightly more accurate than those obtained from the UNSAT2 code. Possible explanation for this is the fact that the UNSAT2 code is based on a finite element formulation in which triangular elements were used to make up rectangular elements, and a diagonalization procedure was used to compute the mass storage matrix [see *Neuman*, 1973; *Neuman et al.*, 1974]. In contrast, the SATURN code is based on the present formulation in which noncomposite rectangular elements with bilinear basis functions and a consistent nondiagonalized mass storage matrix are used. The noncomposite rectangular elements are

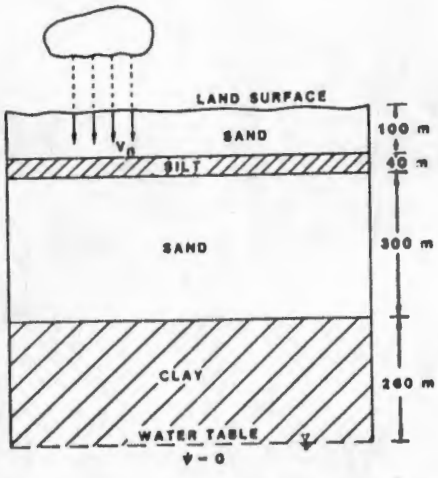

Fig. 8. Schematic description and data for the test problem in example 2.

TABLE 2. Material Properties for the Test Problem in Example 2

Material Type	Saturated Hydraulic Conductivity K, m/yr	Thickness b, m	Porosity ϕ	Specific Storage S_s, m^{-1}	Residual Saturation S_{rw}
Sand	1.06×10^{-2}	100	0.36	0	0.03
Silt	4.02×10^{-3}	40	0.62	0	0.12
Sand	1.06×10^{-2}	300	0.36	0	0.03
Clay	2.85×10^{-4}	260	0.58	10^{-4}	0.26

known to yield a higher order approximation of the head gradient than the linear triangular elements.

To provide further assessment of the numerical results, a plot of pressure head profiles is presented in Figure 6. As expected, the results obtained from both codes are in reasonably good agreement. It should be noted, however, that at later time values the pressure head profiles predicted by the UNSAT2 code tends to be slightly ahead of the profiles predicted by the SATURN code. This behavior of the computed head profiles is indeed consistent with the behavior of the corresponding saturation profiles depicted in Figure 5.

For completeness the computed relations of water influx versus time are also presented. The results obtained using the two codes and different nonlinear solution algorithms are compared in Figure 7 and Table 1, respectively. In Figure 7, the values of water inflow rate obtained from the UNSAT2 code are compared with those obtained from the SATURN code using the Picard algorithm. It is evident that during the first few time steps there are significant discrepancies between the two sets of results. These early time discrepancies may be due to the fact that the storage term of the governing equation is neglected in a certain subroutine of UNSAT2 that computes nodal fluxes. Consequently, the values of the inflow rate predicted by the UNSAT2 code are substantially lower than the values predicted by the SATURN code. The latter normally gives extremely small mass balance errors (of the order of 10^{-10} to 10^{-8}% of the total inflow rate) for this type of problem.

For reference purposes we also compare the performance of the Picard and the Newton-Raphson algorithms described in the present work. It can be seen in Table 1 that the two algorithms produce solutions that are in excellent agreement with each other. In this simulation example, which involves a transient solution of a mildly nonlinear problem, both algorithms required no more than three or four iterations per time step to converge to the final solution within a head tolerance of 0.001 cm. For the majority of the time steps taken the Newton-Raphson algorithm took approximately one iteration less per time step than the Picard algorithm.

TABLE 3. Constitutive Relations and Parameter Values for the Test Problem in Example 2

Material Type	α, m^{-1}	β	γ	a	b	S_{rw}
Sand	1.42	2.62	0.197	−5.	1.	0.03
Silt	8.17×10^{-2}	0.903	1.83	0.	5.566	0.12
Clay	8.63×10^{-3}	0.627	2.83	0.	9.30	0.26

Constitutive relations: $\log_{10} k_{rw} = [aS_e^2 + (b - 2a)S_e + a - b]$; $S_e = 1/[1 + (\alpha|\psi - \psi_a|)^\beta]^\gamma$, where $S_e = (S_w - S_{rw})/(1 - S_{rw})$.

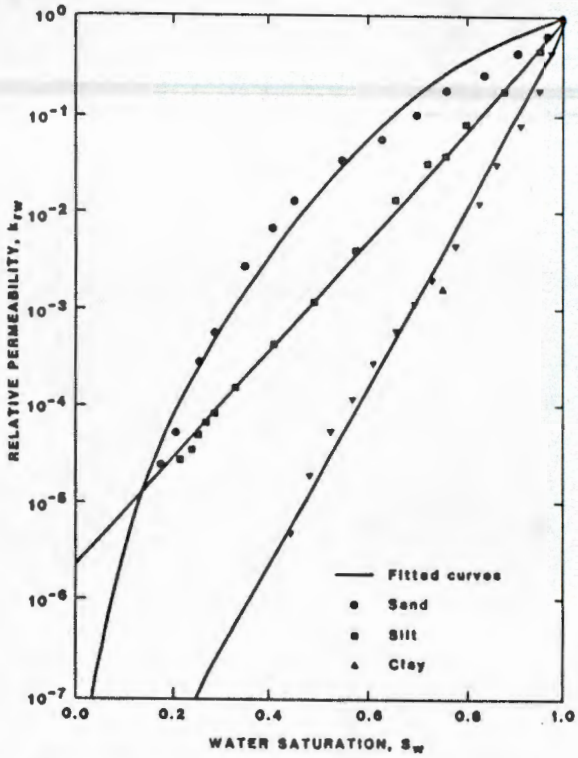

Fig. 9. Relative permeability versus water saturation curves for the test problem in example 2.

Example 2: Vertical Flow in a Multilayered Soil System

The purpose of this example is to test the capability of the proposed nonlinear solution algorithms to handle a field problem involving moisture movement in dessicated soils with highly nonlinear constitutive relations. This type of problem is difficult to solve numerically because, under the stated conditions, the eigenvalues of the coefficient matrix of the physical system are widely spread in magnitude. (For further discussion on the behavior of the matrix equation, see *Finlayson* [1977]). In general, the severity of the numerical problem depends on the degree of variation in the values of the effective hydraulic conductivity and the moisture capacity over the flow region.

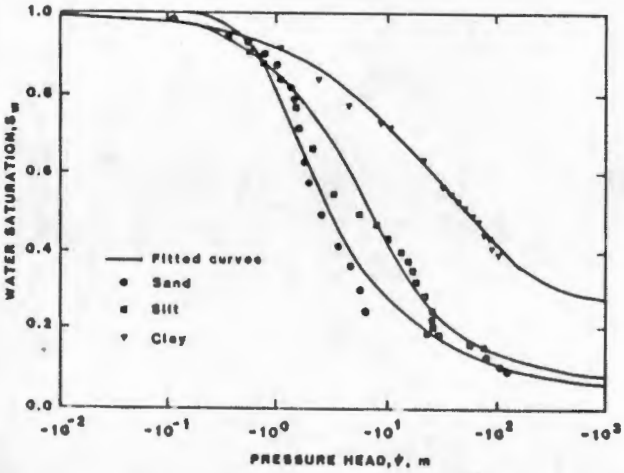

Fig. 10. Water saturation versus pressure head curves for the test problem in example 2.

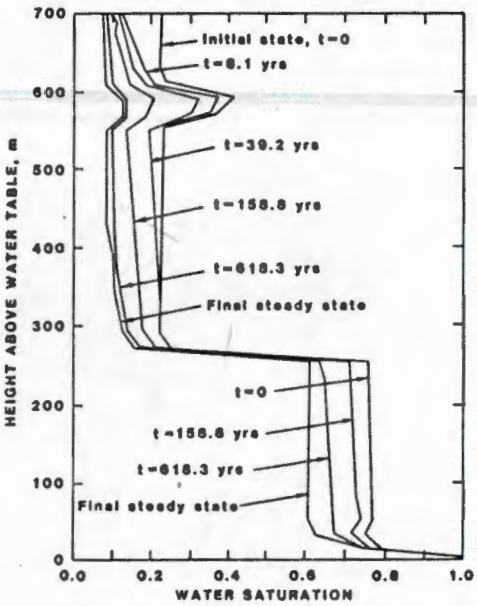

Fig. 11. Water saturation profiles at typical time values.

We focused on a situation concerning infiltration in a multilayered soil system at a site in a semiarid environment. The conceptual flow model is illustrated in Figure 8. To study the transient response of the flow system, a scenario involving a drastic change in recharge rate was used. In this scenario it was assumed that initially the flow system was in a steady state while receiving pluvial recharge at the rate of 0.16 m/yr. Subsequently, the recharge rate was reduced to 0.006 m/yr, and this value was maintained over a long period of time until another steady state condition was established.

A one-dimensional flow simulation was performed using the values of material properties presented in Tables 2 and 3. Soil moisture characteristics used were based on experimental data taken from *Elzeftawy and Cartwright* [1983]. These data are plotted in Figures 9 and 10. Also included in the figures are the curves obtained by using simple analytical functions to fit the experimental data. These functions and their best-fit parameter values are listed in Table 3. It is apparent from examining Figures 9 and 10 that for the expected range of pressure head values, $-1000 \leq \psi \leq 0$ m, the change in the values of relative permeability is up to six orders of magnitude. This is indicative of a severely nonlinear flow condition from the numerical solution standpoint.

To obtain the numerical result, the flow region was represented by a uniform grid consisting of 70 rectangular elements, each having nodal spacings of 1 m and 10 m in the x and y directions, respectively. The initial condition of the transient flow case was derived by performing a steady state analysis using the recharge rate of 0.16 m/yr. The steady state flow computation was performed in one stage using the Newton-Raphson algorithm, which took 10 iterations to converge to a head tolerance of 0.0001 m. (The one-stage steady state analysis was achieved by setting the storage term of (2) to zero, thereby reducing the governing equation to an elliptic equation. Unfortunately, the Picard algorithm did not converge for this steady case.) Following the steady state analysis, a transient flow computation was performed using the derived initial condition and the reduced recharge rate of 0.006 m/yr. Thirty time steps were taken, and the time step values were generated

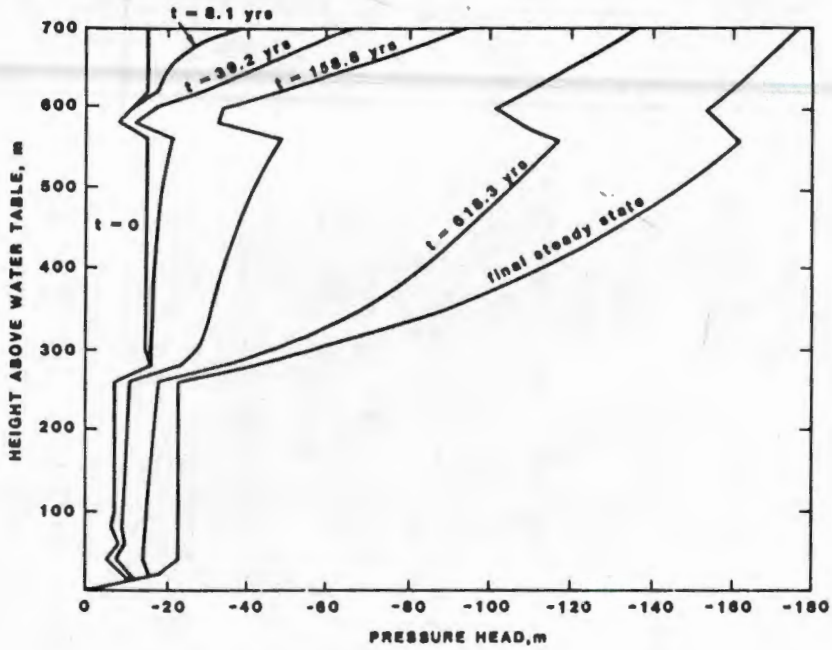

Fig. 12. Pressure head profiles at typical time values.

using the following algorithm: $\Delta t_1 = 1.141$ yr, $\Delta t_k = 1.4\Delta t_{k-1} \leq 500$ yr, for $k = 2, \cdots, 30$. Once again, the Newton-Raphson algorithm gave fast convergence for all time steps. On the average, it took eight iterations per time step to reach the head tolerance of 0.0001 m. The Picard algorithm did not perform as well. At several stages in the solution process it was necessary to reduce the value of the time step by half to obtain convergence within 20 iterations.

The result of the transient flow analysis is presented in Figures 11 and 12, which illustrate the sequences of water saturation and pressure head profiles. It should be noted that the buildup of water saturation and abrupt changes in the pressure head gradients were caused by the presence of the layers of fine silt and clay materials.

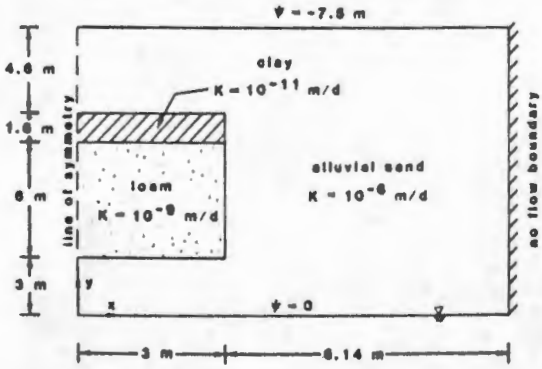

DISCRETIZATION DATA

Δx_i, m $i = 1, \ldots, 9$	0.75, 0.75, 0.75, 0.75, 0.6, 1.2, 1.2, 1.2, 1.34
Δy_j, m $j = 1, \ldots, 16$	1.3, 1.0, 0.6, 1.2, 1.4, 1.4, 1.0, 1.0, 0.6, 0.4, 0.6, 1.2, 1.2, 1.2, 1.0

Fig. 13. Schematic description and data for the test problem in example 3.

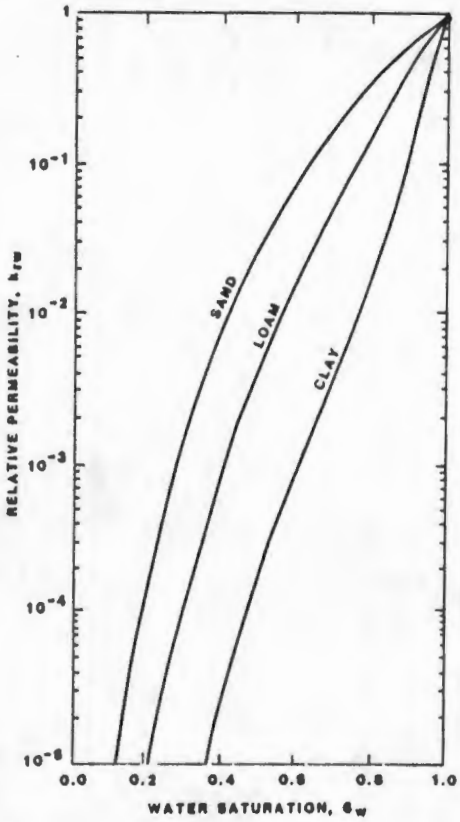

Fig. 14. Relative permeability versus water saturation curves for the test problem in example 3.

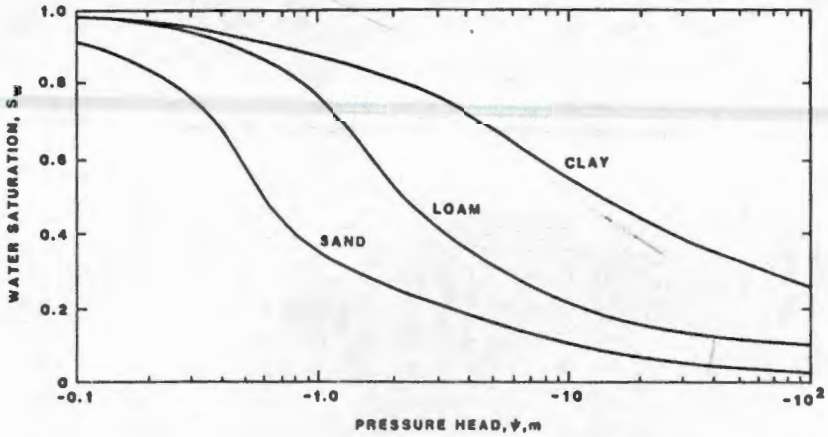

Fig. 15. Water saturation versus pressure head curves for the test problem in example 3.

Example 3: Two-Dimensional Steady Flow in a Formation With Lenticular Deposits

In this example we deal with a two-dimensional simulation of steady state flow in an unsaturated zone above the water table. The problem considered is shown in Figure 13. It is assumed that the alluvial sand formation contains lenses of low-permeability clay and loam. The soil properties used in the simulation are representative of typical unconsolidated materials. Note that the saturated hydraulic conductivity contrast between the fine and coarse materials is up to five orders of magnitude. In addition, each soil material has very highly nonlinear relative permeability and water saturation curves as can be seen in Figures 14 and 15, respectively. Once again, such features of the problem will lead to convergence difficulties unless one uses a numerical solution scheme designed to accomodate not only abrupt changes in the gradients of the constitutive relations but also a wide range of values of effective conductivity.

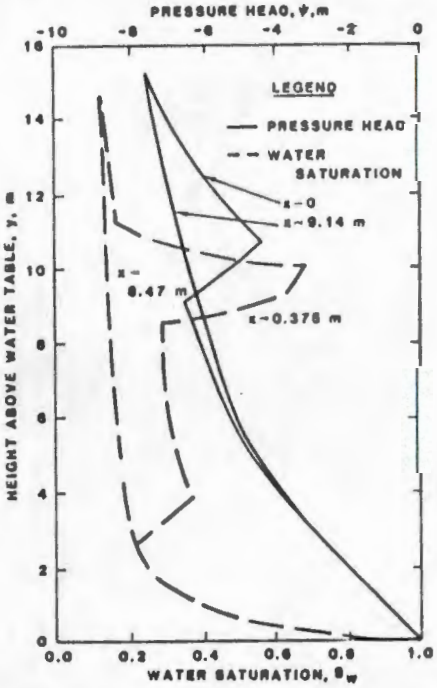

Fig. 16. Steady state water saturation and pressure head profiles.

In order to subject the proposed Picard and Newton-Raphson algorithms to another severe test, the SATURN code was used to perform a one-stage steady state solution using a rectangular grid consisting of 135 elements. The nodal spacings in the x and y directions are given in Figure 13. In this computer run the constitutive relations of k_{rw} versus S_w and S_w versus ψ were supplied to the code in a tabulated form. The iterative solution was initiated by setting the starting value of the pressure head equal to zero and using this in conjunction with linear interpolation of k_{rw} and S_w values to compute the element matrices. Despite this rather poor estimate of ψ, fast convergence to the final answer was obtained with both the Picard and the Newton-Raphson algorithms. The Picard algorithm took 12 iterations and the Newton-Raphson took only eight iterations to achieve convergence within a head tolerance of 10^{-4} m. The final pressure head solutions from both algorithms were found to be in excellent agreement with each other, their maximum difference being less than 0.005 m. To illustrate the effect of the low-permeability lenses on moisture and head distributions, computed values of water saturation and pressure head are plotted in Figure 16. As can be expected, the presence of lenses of fine materials causes a substantial buildup of water saturation and abrupt changes in the pressure gradient at the interfaces of the different materials. These effects are known as capillary perching, which is often encountered when a fine-grained layer overlies a coarser layer.

Example 4: Two-Dimensional Transient Flow in an Unconfined Groundwater System Adjacent to a Landfill

As a final example, a transient simulation of saturated-unsaturated flow in a complex groundwater system adjacent to a landfill site is presented. Data used in this simulation was fabricated using some general information extracted from *Silka and Mercer* [1982]. The cross section analyzed is depicted in Figure 17. Three distinct layers are considered. The top layer is made of a loam material, whereas the middle and the lower layers are made up of dessicated clay and a mixture of clay and till, respectively. The landfill site corresponds to a canal which is presently backfilled with the loam and clay materials. There exists a semipermeable clay cap, extending over 125 m length from the center of the landfill, which corresponds to the right vertical boundary of the flow region. To control the water table position, a tile drain was placed at 100

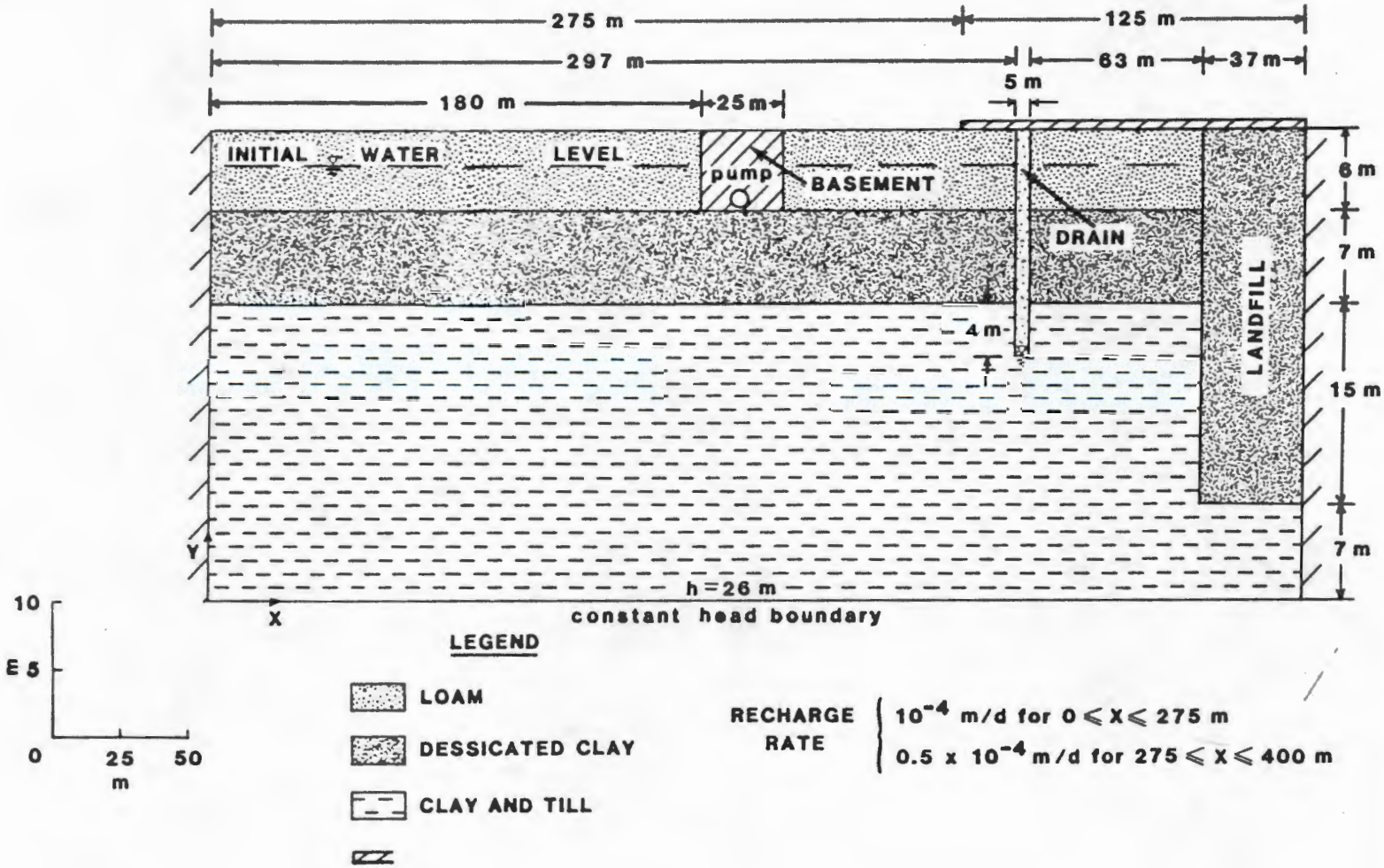
275 m
125 m
297 m
63 m
37 m
180 m
25 m
5 m
INITIAL WATER LEVEL
pump
BASEMENT
DRAIN
LANDFILL
6 m
7 m
15 m
7 m
4 m
h = 26 m
constant head boundary
X
Y
10
E 5
0
25
50
m
LEGEND
LOAM
DESSICATED CLAY
CLAY AND TILL
RECHARGE RATE
10^{-4} m/d for $0 \leq X \leq 275$ m
0.5×10^{-4} m/d for $275 \leq X \leq 400$ m

TABLE 4. Material Properties for the Test Problem in Example 4

Material Type	K, m/d	ϕ	S_s, m^{-1}
Loam	5×10^{-2}	0.45	10^{-3}
Dessicated clay	5×10^{-3}	0.60	2×10^{-3}
Clay and till	5×10^{-4}	0.60	2×10^{-3}

TABLE 5. Constitutive Relations and Parameter Values for the Test Problem in Example 4

Material	S_{wr}	n	α, m^{-1}	β	γ
Loam	0.05	2	0.5	2	1.
Dessicated clay	0.20	2	0.282	1.5	1.
Clay and till	0.20	2	0.282	1.5	1.

Constitutive relations: $(S_w - S_{wr}) = (1 - S_{wr})/[1 + (\alpha|\psi - \psi_d|)^\beta]^\gamma$; $k_{rw} = (S_w - S_{wr})^n/(1 - s_{wr})^n$.

m from the right vertical boundary. In addition, a pump was also placed in the basement of a building located at a distance of 207.5 m from the right vertical boundary of the landfill. This pump is normally put into operation whenever the water level in the basement lies above the bottom of the basement.

The initial condition for this problem corresponds to a static water level 32 m above the base of the clay and till layer. The boundary conditions are as shown in Figure 17. Note that the water level in the drain is fixed at 4 m below the base of the dessicated clay layer, and when the pump is in operation, the water level in the basement is fixed at 6 m from the top. Vertical recharge is applied to the top boundary at two different rates, as depicted in Figure 17.

The soil material properties used in the simulation are given in Table 4. Functional constitutive relations were selected, and these are listed in Table 5. The function of water saturation versus pressure head was taken from *van Genuchten et al.* [1977], whereas the function of relative permeability versus water saturation was taken from *Brooks and Corey* [1964] and *Mualem* [1976]. Although the constitutive relations used in this example are not as highly nonlinear as those used in the two previous examples, the present simulation is probably as difficult as the previous simulations. This is because in the present case it is necessary to accomodate sudden and large changes of head values at the drain and the basement boundaries, as well as drastic changes of gradients of the nonlinear functions at certain saturated nodes which become unsaturated.

Using the given physical parameter values and a moderately fine mesh consisting of 252 nodes and 225 elements (216 rectangles and nine triangles), the problem was solved for 40 time steps. The time step values were computed using the following algorithm: $\Delta t_1 = 1$ d, $\Delta t_k = 1.414$, $\Delta t_{k-1} \leq 600$ d, $k = 2, \cdots, 40$. The seepage face boundary condition at the drain was treated in a simple manner using a trial-and-error procedure similar to that given by *Neuman et al.* [1974]. For most of the time the Picard algorithm took four or five iterations per time step, whereas the Newton-Raphson algorithm took three iterations to converge within a head tolerance of 10^{-4} m. Both nonlinear algorithms produced pressure head solutions which were very close to each other. To show the effects of drainage and pumping on the flow system, the hydraulic head profiles along $y = 18.5$ m and $y = 29$ m are plotted in Figures 18 and 19, respectively. Note that there is quite a significant difference between head values at the two elevations. This indicates significant vertical flow, particularly in the vicinity of the tile drain. Also evident is the influence of pumping at the basement. This causes the reversal of the hydraulic gradient in the horizontal plane, y = 18.5 m, and from the tile drain toward the basement.

Finally, a plot showing temporal variation of the drain flux is presented in Figure 20. Once again, it is apprarent that the Picard and the Newton-Raphson algorithms produced virtually identical results. The drain flux curve approaches the steady state value asympototically, which implies a long-time attainment of equilibrium between the withdrawal and the replenishment of water in the flow system.

CONCLUSIONS

The examples and numerical results presented demonstrate clearly that the Galerkin finite element formulation developed in this work is effective in handling severely nonlinear cases of variably-saturated flow. The most significant features of the present formulation are the Picard and the Newton-Raphson algorithms, as well as the influence coefficient technique for element matrix computation.

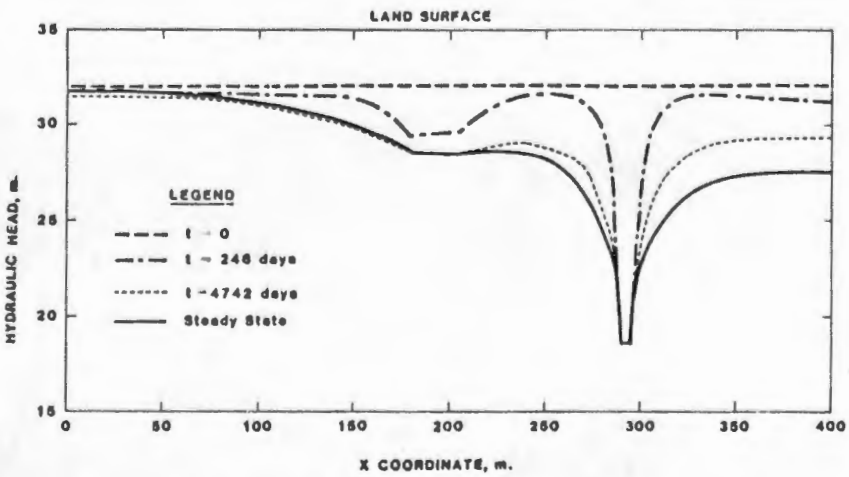

Fig. 18. Hydraulic head distributions along $y = 18.5$ m.

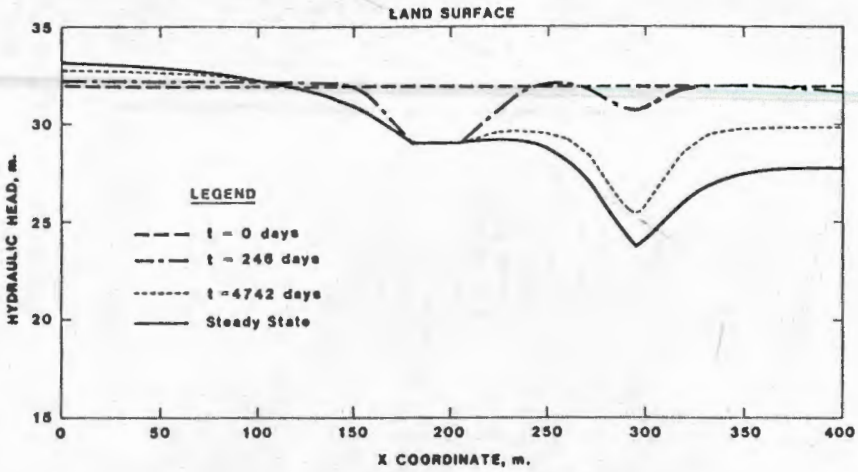

Fig. 19. Hydraulic head distributions along $y = 29$ m.

It has been shown that the influence coefficient matrix generation scheme is extremely simple to implement and requires very little computational effort in the element matrix evaluation. Typically, for rectangular elements, we estimate via arithmetic operation counts that the influence coefficient scheme requires no more than 5% of the CPU time required by the Gauss quadrature numerical integration scheme, using 2×2 Gauss points.

One important feature of the two solution algorithms employed is the use of a chord slope formula for the evaluation of the gradient of the soil moisture characteristic curves. It has been shown that such a procedure can greatly enhance the convergence properties of the iterative solution process as well as the stability of the numerical solution. Good results were obtained even in cases for which the elements of the global coefficient matrix differ by more than five orders of magnitude. (Such behavior of the coefficient matrix is usually caused by large variations in the effective hydraulic conductivity and specific moisture capacity).

A comparative study of the Picard and Newton-Raphson algorithms led to the following conclusions:

1. The Picard scheme requires less CPU time per iteration than the Newton-Raphson scheme. This is because the latter scheme produces an asymmetric coefficient matrix which requires more computational effort to reduce.

2. Despite its greater cost per iteration, the Newton-Raphson algorithm can be comparable in overall cost because it is more strongly convergent and normally requires a smaller number of iterations than its counterpart. This is particularly true in steady state simulations.

3. In certain cases it becomes difficult to obtain convergence using the Picard scheme, as was illustrated in example 2. For such cases it is necessary to employ the Newton-Raphson scheme to obtain a solution in a cost-effective manner.

4. For each of the problems considered, the numerical results obtained from the two solution algorithms were almost identical, provided that the same spatial and temporal discretization were employed.

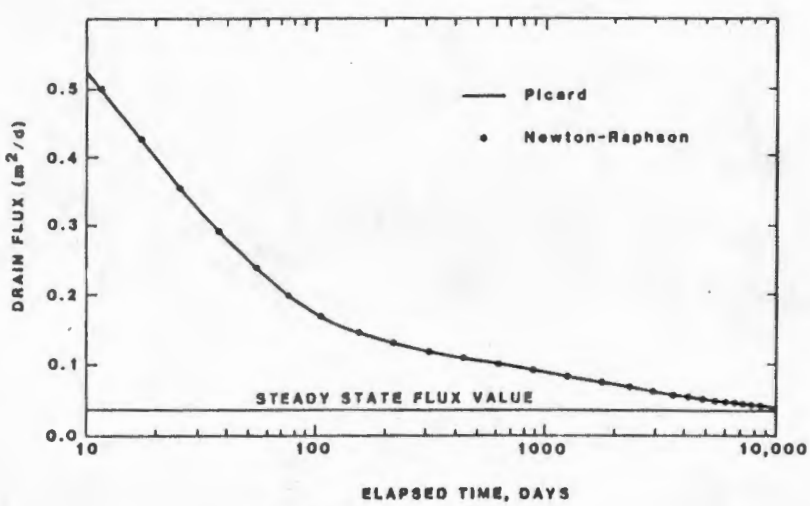

Fig. 20. Drain flux versus time.

APPENDIX A: INFLUENCE COEFFICIENT MATRICES $[A^{xx}]^e$, $[A^{yy}]^e$, $[M]^e$, AND $\{F_y\}^e$ OF THE LINEAR RECTANGULAR ELEMENT

$$[A^{xx}]^e = \frac{1}{6}\begin{bmatrix} 2 & -2 & -1 & 1 \\ -2 & 2 & 1 & -1 \\ -1 & 1 & 2 & -2 \\ 1 & -1 & -2 & 2 \end{bmatrix}$$

$$[A^{yy}]^e = \frac{1}{6}\begin{bmatrix} 2 & 1 & -1 & -2 \\ 1 & 2 & -2 & -1 \\ -1 & -2 & 2 & 1 \\ -2 & -1 & 1 & 2 \end{bmatrix}$$

$$[M]^e = \frac{1}{9}\begin{bmatrix} 4 & 2 & 1 & 2 \\ 2 & 4 & 2 & 1 \\ 1 & 2 & 4 & 2 \\ 2 & 1 & 2 & 4 \end{bmatrix}$$

$$\{F_y\}^e = \begin{Bmatrix} -1 \\ -1 \\ 1 \\ 1 \end{Bmatrix}$$

APPENDIX B: INFLUENCE COEFFICIENT MATRICES $[A^{xx}]^e$, $[A^{yy}]^e$, $[M]^e$, AND $\{F_y\}^e$ OF THE LINEAR RECTANGULAR ELEMENT

$$[A^{xx}]^e = \begin{bmatrix} \beta_1\beta_1 & \beta_1\beta_2 & \beta_1\beta_3 \\ \beta_2\beta_1 & \beta_2\beta_2 & \beta_2\beta_3 \\ \beta_3\beta_1 & \beta_3\beta_2 & \beta_3\beta_3 \end{bmatrix}$$

$$[A^{yy}]^e = \begin{bmatrix} \gamma_1\gamma_1 & \gamma_1\gamma_2 & \gamma_1\gamma_3 \\ \gamma_2\gamma_1 & \gamma_2\gamma_2 & \gamma_2\gamma_3 \\ \gamma_3\gamma_1 & \gamma_3\gamma_2 & \gamma_3\gamma_3 \end{bmatrix}$$

$$[M]^e = \frac{1}{4}\begin{bmatrix} 2 & 1 & 1 \\ 1 & 2 & 1 \\ 1 & 1 & 2 \end{bmatrix}$$

$$\{F_y\}^e = \begin{Bmatrix} \gamma_1 \\ \gamma_2 \\ \gamma_3 \end{Bmatrix}$$

$$\beta_1 = (y_2' - y_3')/2\Delta \qquad \beta_2 = y_3'/2\Delta$$

$$\beta_3 = -y_2'/2\Delta \qquad \gamma_1 = (x_3' - x_2')/2\Delta$$

$$\gamma_2 = -x_3'/2\Delta \qquad \gamma_3 = x_2'/2\Delta$$

$$\Delta = (x_2'y_3' - x_3'y_2')/2$$

APPENDIX C: INFLUENCE COEFFICIENT MATRICES $[A^*]^e$, $[B^*]^e$, AND $[F^*]^e$ OF THE LINEAR RECTANGULAR ELEMENT

$$[A^*]^e = \begin{bmatrix} a_1^* & a_1^* & a_1^* & a_1^* \\ a_2^* & a_2^* & a_2^* & a_2^* \\ a_3^* & a_3^* & a_3^* & a_3^* \\ a_4^* & a_4^* & a_4^* & a_4^* \end{bmatrix}$$

$$[F^*]^e = -\tfrac{1}{2}\langle k_{rw}'\rangle K_{yy} l \begin{bmatrix} 1 & 1 & 1 & 1 \\ 1 & 1 & 1 & 1 \\ 1 & 1 & 1 & 1 \\ 1 & 1 & 1 & 1 \end{bmatrix}$$

$$[B^*]^e = \left(\frac{lm}{36}\right)\left(\frac{S_s\bar{S}_w}{\Delta t_k}\right)\begin{bmatrix} 4 & 2 & 1 & 2 \\ 2 & 4 & 2 & 1 \\ 1 & 2 & 4 & 2 \\ 2 & 1 & 2 & 4 \end{bmatrix} + \left(\frac{\phi lm}{16\Delta t_k}\right)\left(\frac{d\bar{S}_w}{d\bar{\psi}}\right)\begin{bmatrix} 1 & 1 & 1 & 1 \\ 1 & 1 & 1 & 1 \\ 1 & 1 & 1 & 1 \\ 1 & 1 & 1 & 1 \end{bmatrix}$$

where

$$a_1^* = \langle k_{rw}'\rangle \frac{K_{xx}m}{6l}(2\psi_1 - 2\psi_2 - \psi_3 + \psi_4) + \frac{K_{yy}l}{6m}(2\psi_1 + \psi_2 - \psi_3 - 2\psi_4)$$

$$a_2^* = \langle k_{rw}'\rangle \frac{K_{xx}m}{6l}(-2\psi_1 + 2\psi_2 + \psi_3 - \psi_4) + \frac{K_{yy}l}{6m}(\psi_1 + 2\psi_2 - 2\psi_3 - \psi_4)$$

$$a_3^* = \langle k_{rw}'\rangle \frac{K_{xx}m}{6l}(-\psi_1 + \psi_2 + 2\psi_3 - 2\psi_4) + \frac{K_{yy}l}{6m}(-\psi_1 - 2\psi_2 + 2\psi_3 + \psi_4)$$

$$a_4^* = \langle k_{rw}'\rangle \frac{K_{xx}m}{6l}(\psi_1 - \psi_2 - 2\psi_3 + 2\psi_4) + \frac{K_{yy}l}{6}(-2\psi_1 - \psi_2 + \psi_3 + 2\psi_4)$$

$$\langle k_{rw}'\rangle = \frac{1}{4}\left(\frac{dk_{rw}}{d\bar{S}_w}\right)\left(\frac{d\bar{S}_w}{d\bar{\psi}}\right)$$

APPENDIX D: INFLUENCE COEFFICIENT MATRICES $[A^*]^e$, $[B^*]^e$, AND $[F^*]^e$ OF THE LINEAR RECTANGULAR ELEMENT

$$[A^*]^e = \begin{bmatrix} a_1^* & a_1^* & a_1^* \\ a_2^* & a_2^* & a_2^* \\ a_3^* & a_3^* & a_3^* \end{bmatrix}$$

$$[B^*]^e = \frac{\Delta}{12}\left(\frac{S_s\bar{S}_w}{\Delta t_k}\right)\begin{bmatrix} 2 & 1 & 1 \\ 1 & 2 & 1 \\ 1 & 1 & 2 \end{bmatrix} + \frac{\phi\Delta}{9\Delta t_k}\left(\frac{d\bar{S}_w}{d\bar{\psi}}\right)\begin{bmatrix} 1 & 1 & 1 \\ 1 & 1 & 1 \\ 1 & 1 & 1 \end{bmatrix}$$

$$[F^*]^e = \begin{bmatrix} F_1^* & F_1^* & F_1^* \\ F_2^* & F_2^* & F_2^* \\ F_3^* & F_3^* & F_3^* \end{bmatrix}$$

where

$$a_1^* = \Delta\langle k_{rw}'\rangle[K_{xx}(\beta_1\beta_1\psi_1 + \beta_1\beta_2\psi_2 + \beta_1\beta_3\psi_3) + K_{yy}(\gamma_1\gamma_1\psi_1 + \gamma_1\gamma_2\psi_2 + \gamma_1\gamma_3\psi_3)]$$

$$a_3^* = \Delta\langle k_{rw}'\rangle[K_{xx}(b_3b_1\psi_1 + b_3b_2\psi_2 + b_3b_3\psi_3) + K_{yy}(c_3c_1\psi_1 + c_3c_2\psi_2 + c_3c_3\psi_3)]$$

$$a_2^* = \Delta\langle k_{rw}'\rangle[K_{xx}(b_2b_1\psi_1 + b_2b_2\psi_2 + b_2b_3\psi_3) + K_{yy}(c_2c_1\psi_1 + c_2c_2\psi_2 + c_2c_3\psi_3)]$$

$$F_1^* = \Delta\langle k_{rw}'\rangle K_{yy}\gamma_1 \qquad F_2^* = \Delta\langle k_{rw}'\rangle K_{yy}\gamma_2$$

$$F_3^* = \Delta\langle k_{rw}'\rangle K_{yy}\gamma_3 \qquad \langle k_{rw}'\rangle = \frac{1}{3}\left(\frac{d\bar{k}_{rw}}{d\bar{S}_w}\right)\left(\frac{d\bar{S}_w}{d\bar{\psi}}\right)$$

APPENDIX E: CONSTITUTIVE RELATIONS AND DISCRETIZATION PARAMETERS FOR THE TEST PROBLEM IN EXAMPLE 1

Constitutive Relations

$$k_{rw} = (S_w - S_{wr})/(1 - S_{wr})$$

$$(\psi - \psi_a)/(\psi_r - \psi_a) = (1 - S_w)/(1 - S_{wr})$$

where

$$S_{wr} = 0.333 \qquad \psi_r = -100 \text{ cm} \qquad \psi_a = 0 \text{ cm}$$

Discretization Parameters

Uniform nodal spacing and time step,

$$\Delta x = 1 \text{ cm} \qquad \Delta t = 0.01 \text{ d}$$

NOTATION

- A_{IJ}^e element matrix for the Picard iterative method.
- B solution boundary.
- B_1 prescribed head boundary.
- B_2 prescribed flux boundary.
- B^e element boundary.
- B_{IJ}^e element matrix for the Picard iterative method.
- e_j unit vector in the x_2 direction.
- F_I^e element right-hand-side vector.
- h_I hydraulic head at node I, L.
- i, j coordinate subscripts.
- I, J, L nodal subscripts.
- k_{rw} relative permeability with respect to the water phase.
- $\bar{k}_{rw}$ relative permeability at centroid of element.
- k time level index.
- K_{ij} saturated hydraulic conductivity tensor, LT^{-1}.
- l, m dimensions of rectangular element, L.
- l length of boundary segment, L.
- $[M]^e$ influence coefficient matrix.
- n number of nodes in the finite element network.
- n_i outward unit normal vector.
- n_w number of wells.
- N_I, N_J basis functions.
- q volumetric flow rate per unit volume of the medium, T^{-1}.
- Q^*, Q_I volumetric rate of well injection at node I, L^3T^{-1}.
- R solution domain.
- R^e element subdomain.
- S_s specific storage, L^{-1}.
- S_w water saturation.
- $\bar{S}_w$ centroidal value of water saturation.
- t elapsed time, T.
- u_I matrix elements equal to 1 for $I = 1$ through 4.
- U_{IJ} matrix elements equal to 1 for all I and J.
- V_i flow velocity in the x_i direction, LT^{-1}.
- V_n Darcy flux at the boundary, LT^{-1}.
- x_i component of the Cartesian coordinate system, L.
- β_I geometric property of a triangular element in the x direction, L^{-1}.
- δ Dirac delta function.
- Δ area of a triangular element, L^2.
- η overall storage coefficient, L^{-1}.
- γ_I geometric property of a triangular element in the y direction, L^{-1}.
- ω time weighting factor.
- ϕ porosity.
- ψ pressure head, L.
- $\bar{\psi}$ prescribed boundary pressure head, L.
- ψ_0 initial pressure head, L.
- $\bar{\psi}$ pressure head at centroid of element, L.

REFERENCES

Braester, C., G. Dagan, S. P. Neuman, and D. Zaslavsky, A survey of the equations and solutions of unsaturated flow in porous media, *First Annu. Rep. Project A10-SWC-77*, 176 pp., Hydraul. Eng. Lab., Technion, Haifa, Israel, 1971.

Brooks, R. H., and A. T. Corey, Hydraulic properties of porous media, *Hydrol. Pap. 3*, 27 pp., Color. State Univ., Fort Collins, 1964.

Bruch, J. C. Two-dimensional unsteady water flow in unsaturated porous media, *Proceedings of the First International Conference on Finite Elements in Water Resources*, edited by W. G. Gray, G. F. Pinder, and C. Brebbia, pp. 3.3-3.19, Pentech, London, 1977.

Brutsaert, W. F., A functional iteration technique for solving the Richards equation applied to two-dimensional infiltration problems, *Water Resour. Res.*, *7*(6), 1583-1596, 1971.

Cooley, R. L., A finite difference method for unsteady flow in variably saturated porous media: Application to a single pumping well, *Water Resour. Res.*, *7*(6), 1607-1625, 1971.

Cooley, R. L., Some new procedures for numerical solution of variably-saturated flow problems, *Water Resour. Res.*, *19*(5), 1271-1285, 1983.

Elzeftawy, A. and K. Cartwright, Undisturbed core method for determining and evaluating the hydraulic conductivity of unsaturated sediments, *Rep. UILU-WRC-83-0177*, 49 pp., Ill. State Geol. Surv., Springfield, 1983.

Finlayson, B. A., Water movement in dessicated soils, *Proceedings of the First International Conference on Finite Elements in Water Resources*, edited by W. G. Gray, G. F. Pinder, and C. Brebbia, pp. 3.91-3.106, Pentech, London, 1977.

Frind, E. O., R. W. Gilham, and J. F. Pickens, Application of unsaturated flow properties in the design of geologic environments for radioactive waste storage facilities, *Proceedings of the First International Conference on Finite Elements in Water Resources*, edited by W. G. Gray, G. F. Pinder, and C. Brebbia, pp. 3.133-3.163, Pentech, London, 1977.

Huyakorn, P. S., and G. F. Pinder, *Computational Methods in Subsurface Flow*, Academic, New York, 1983.

Mualem, Y., A new model for predicting the hydraulic conductivity of unsaturated porous media, *Water Resour. Res.*, *12*(3), 513-522, 1976.

Neuman, S. P., Saturated-unsaturated seepage by finite elements, *J. Hydraul. Div. Am. Soc. Civ. Eng.*, *99*(HY12), 2233-2250, 1973.

Neuman, S. P., R. A. Feddes, and E. Bresler, Finite element simulation of flow in saturated-unsaturated soils considering water uptake by plants, *Rep. Project ALO-SWC-77*, 104 pp., Hydrodyn. and Hydraul. Eng. Lab., Technion, Haifa, Israel, 1974.

Philip, J. R., Numerical solution of equations of the diffusion type with diffusivity concentration-dependent, *Trans. Faraday Soc.*, *51*, 885-892, 1955.

Philip, J. R., Theory of infiltration, *Adv. Hydrosci.*, *5*, 216-291, 1969.

Reeves, M., and J. O. Duguid, Water movement through saturated-unsaturated porous media: A finite-element Galerkin model, *Rep. ORNL-4927*, Oak Ridge Nat. Lab., Oak Ridge, Tenn., 1976.

Richards, L. A., Capillary conduction of liquids through porous mediums, *Physics*, *1*, 318–333, 1931.

Silka, L. R., and J. W. Mercer, Evaluation of remedial actions for groundwater contamination at Love Canal, New York, paper presented at the National Conference on Management of Uncontrolled Hazardous Waste Sites, Hazardous Mater. Contr. Res. Inst., Silver Spring, Md., 1982.

van Genuchten, M. Th., G. F. Pinder, and W. P. Saukin, Modeling of leachate and soil interactions in an aquifer, Management of Gas and Leachate in Landfills, *Rep. EPA-600/9-77-026*, pp. 95–103, U.S. Environmental Protection Agency, Cincinnati, Ohio, 1977.

Yeh, G. T., On the computation of Darcian velocity and mass balance in the finite element modeling of groundwater flow, *Water Resour. Res.*, *17*(5), 1529–1534, 1981.

Yeh, G. T., and D. S. Ward, FEMWATER: A finite-element model of water flow through saturated-unsaturated porous media, *Rep. ORNL-5567*, Oak Ridge Nat. Lab., Oak Ridge, Tenn., 1980.

Yeh, G. T., and D. S. Ward, FEMWASTE: A finite-element model of waste transport through saturated-unsaturated porous media, *Rep. ORNL-5601*, Oak Ridge Nat. Lab., Oak Ridge, Tenn., 1981.

P. S. Huyakorn and S. D. Thomas, GeoTrans Inc., P. O. Box 2550, Reston, VA 22090.

B. M. Thompson, Intera, 11999 Katy Freeway, Houston, TX 77079.

(Received October 10, 1983;
revised April 13, 1984;
accepted April 23, 1984.)

92124171705